Vacuum 179 (2020) 109515

Contents lists available at ScienceDirect

Vacuum

journal homepage: http://www.elsevier.com/locate/vacuum

Microstructure evolution of thermo-mechanically affected zone in dissimilar AA2024/7075 joint produced by friction stir welding

Chenghang Zhang [a,b], Guangjie Huang [a,b,*], Yu Cao [a,b,**], Yulong Zhu [a,b], Xinde Huang [a,b], Yi Zhou [a,b], Qilei Li [a,b], Qinghui Zeng [c], Qing Liu [d]

[a] International Joint Laboratory for Light Alloys (MOE), College of Materials Science and Engineering, Chongqing University, Chongqing, 400044, PR China
[b] Shenyang National Laboratory for Materials Science, Chongqing University, Chongqing, 400044, PR China
[c] College of Mechanical and Electrical Engineering, Chongqing University of Arts and Sciences, Chongqing, 402160, PR China
[d] College of Materials Science and Engineering, Nanjing Tech University, Nanjing, 211816, PR China

ARTICLE INFO

Keywords:
Friction stir welding
Aluminum alloys
Microstructure
Texture
Hardness

ABSTRACT

In the present research, the microstructure characterization of the thermo-mechanically affected zone (TMAZ) in dissimilar FSW AA2024/7075 joint was systematically investigated. The results showed that many Cu-rich and Zn-rich constituent particles are generated in the TMAZ on the advancing side (AS-TMAZ) and the retreating side (RS-TMAZ), respectively. This mainly depends on the corresponding base materials (BMs) at the AS and RS. The precipitated particles are coarsened in the AS-TMAZ and RS-TMAZ compared to the corresponding BMs owing to the thermal cycle produced during FSW. Grain bending occurs in the TMAZ, and the degree of grain curvature in the RS-TMAZ are more pronounced than that in the AS-TMAZ. Many dislocations and sub-grains including a large number of LAGBs can be found in the AS-TMAZ and RS-TMAZ. The entire texture intensity is stronger in the AS-TMAZ and weaker in the RS-TMAZ as compared to the corresponding BMs. The original texture components are changed and some new shear components can be produced as a result of the severe shear deformation during FSW. The hardness value of the AS-TMAZ and RS-TMAZ is lower than that of the corresponding BMs due to the precipitated particles coarsening during FSW.

1. Introduction

Joining of dissimilar aluminum alloys has been a major challenge because of the differences in physical, chemical, metallurgical and mechanical properties, especially for the heat treatable ones (2xxx, 6xxx and 7xxx) due to their sensitivity to temperature [1–3]. As common structural components, 2xxx and 7xxx alloys are usually applied in the parts of aircraft wings [4]. In the fabrication of such structural materials, the dissimilar welding of 2xxx and 7xxx alloys is difficult via traditional fusion methods. This is because the heat input generated results in the dramatic loss of strength resulting from the thermal softening mechanism. Furthermore, some defects, such as cracks and voids, can be produced by fusion welding [5–8]. Contamination of the shielding gas results in weld instability, oxidation and porosity in the gas tungsten arc welding [9], which has also been proved by Siewert et al. [10]. Moreover, they found that the turbulences surrounding the arc and turbulences in the effluent hot gas can not be clearly distinguished at the gas flow rates of less than 30 L/min through measurement. Electron beam welding have also found application in welding, however, it is likely to have a greater tendency towards pore formation as the necessary high vacuum (e.g. 10^{-6} mbar) might not be achieved under the extensive gas contamination [11]. Accordingly, it is essential to reduce or eliminate these problems by adopting new welding methods.

Friction stir welding (FSW) technology, patented by TWI in 1991, has been successfully used to produce the ideal joint. The welding defects, such as hot cracking, large distortion and porosity can be avoided by FSW [12,13], due to the fact that the operating temperature is below the melting temperature of the base materials (BMs) [14–16]. Since the residual gas contamination can not be produced during FSW [17,18], it is also an environmental protection technology [5]. It has been

* Corresponding author. International Joint Laboratory for Light Alloys (MOE), College of Materials Science and Engineering, Chongqing University, Chongqing, 400044, PR China.
** Corresponding author. International Joint Laboratory for Light Alloys (MOE), College of Materials Science and Engineering, Chongqing University, Chongqing, 400044, PR China.
E-mail addresses: gjhuang@cqu.edu.cn (G. Huang), yucao928@cqu.edu.cn (Y. Cao).

https://doi.org/10.1016/j.vacuum.2020.109515
Received 28 March 2020; Received in revised form 24 May 2020; Accepted 25 May 2020
Available online 10 June 2020

Table 1
Chemical composition of the aluminum alloys (in wt.%).

	Si	Fe	Cu	Mn	Mg	Cr	Zn	Ti	Al
2024-T351	0.05	0.17	4.5	0.6	1.4	0.01	0.03	0.02	Bal.
7075-T651	0.05	0.19	1.7	0.04	2.4	0.2	5.8	0.03	Bal.

documented that the mechanical properties of the joints produced by FSW are better than those of the fusion welded joints so that it becomes more mature and popular in the welding of aluminum alloys [15]. In recent years, it has received extensive attention and become a popular research topic in domestic and overseas [19]. FSW plays a big role in joining of various metals and alloys, especially for aluminum alloys. Accordingly, understanding the microstructure development is of great significance to analyze the mechanical properties of the FSW joints.

Generally, different microstructural zones can be found in the FSW joints [20,21], i.e., stir zone or nugget zone (NZ), thermo-mechanically affected zone (TMAZ) and heat affected zone (HAZ). The FSW joints of aluminum alloys are usually fractured at the boundaries in the TMAZ and the NZ on the advancing side (AS) or the welded zone [22–24]. Accordingly, many researches mainly focus on these welded zone of the FSW joints. Mahoney et al. [25] and Liu and Ma [26] reported that the fraction location of the FSW joints is in the HAZ, which is the low hardness region. The hardness change mainly depends on the formation state of the precipitated phases. Chen et al. [23] found that all the joints are fractured in the boundaries between the NZ and TMAZ on the AS, resulting from the dislocations pinned by the precipitates and the abrupt change of the microstructure on the AS. Rhodes et al. [27] put forward that the precipitates are dissolved or reduced in the NZ. Liu et al. [28] reported that extensive precipitates are re-precipitated in the NZ at high heat input. Chen and Jiang [29] concluded that the strain induced grain boundary migration results in the formation of the Cube texture and enhancement of the recrystallization texture. Wang et al. demonstrate that the complex structure of the two materials with flowing shape is presented in the NZ, which is mainly made up of the material on the AS. Furthermore, shear texture is produced in the NZ due to the presence of shear deformation. Moradi et al. [2] found that the precipitate fraction in the NZ of the retreating side (RS) is significantly higher than that of

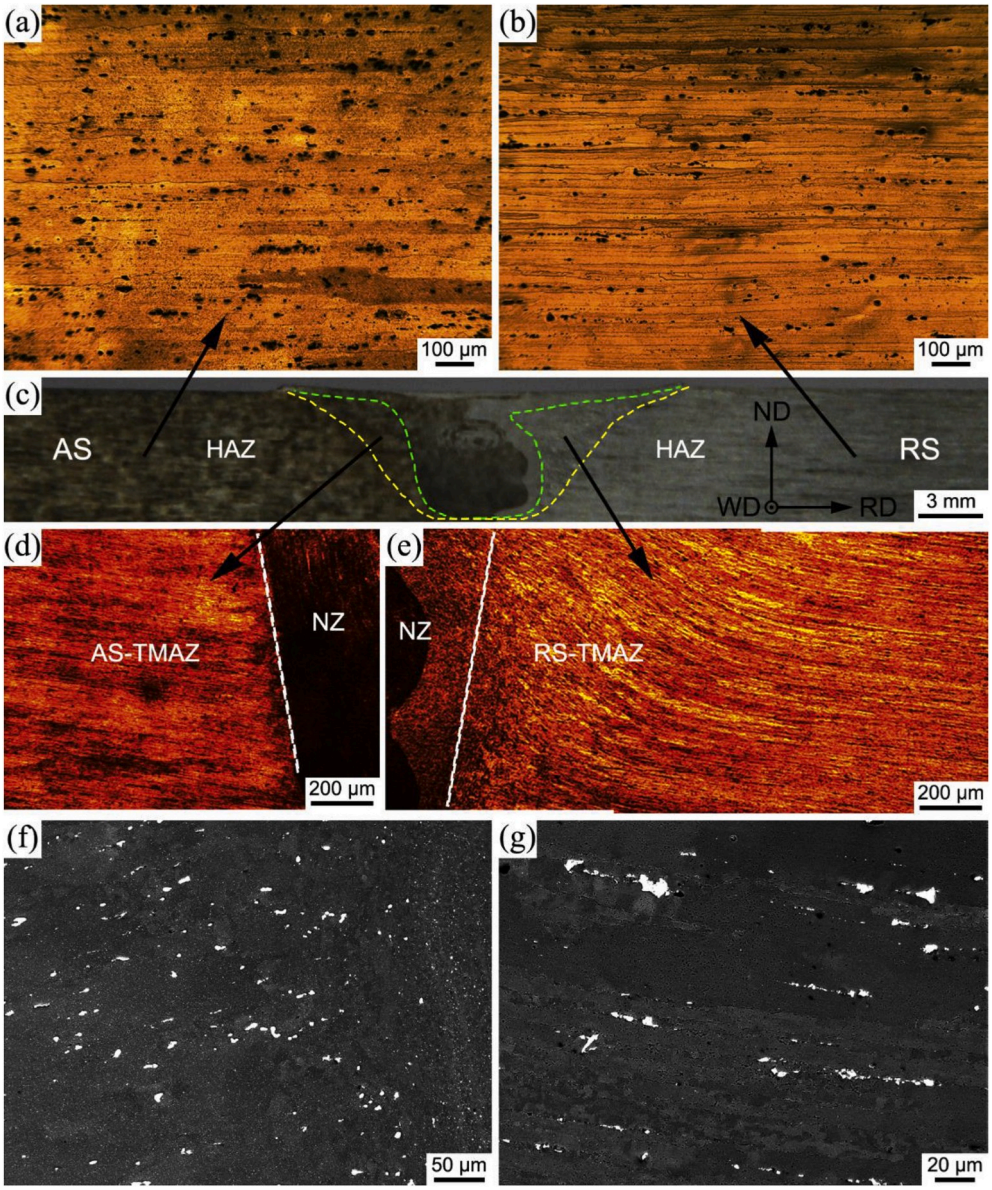

Fig. 1. Morphology of the BMs of the dissimilar FSW joint (a) OM images of AA2024 BM, (b) OM images of AA7075 BM, (c) macro appearance of the joint, (d) AS-TMAZ, (e) RS-TMAZ, (f) SEM images of AS-TMAZ and (f) SEM images of RS-TMAZ.

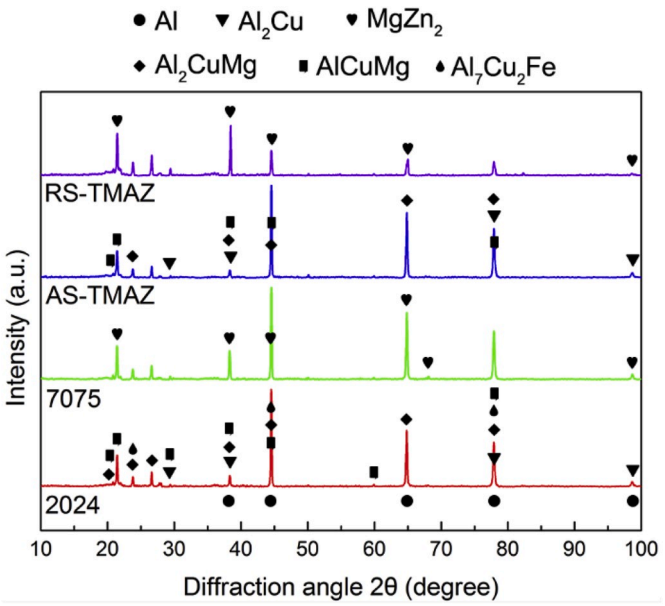

Fig. 2. XRD patterns of the BMs and the TMAZ on the AS and RS of the dissimilar FSW joint.

the AS. And the low extent of continuous dynamic recrystallization occurs in the TMAZ of the AS compared to that of the RS.

Although some works are available on the microstructure of the FSW joints, there is still lack of in-depth understanding of the microstructure in the welded zone of the joints, in particular for dissimilar joints. Consequently, the objective of this study is to investigate the microstructure characterization of the TMAZ in the dissimilar FSW AA2024/7075 joint referring to the optimal welding parameters in the precious research [30]. Multiple characterization methods, such as X-ray diffractometer (XRD), scanning electron microscopy equipped with an energy dispersive spectroscopy (SEM/EDS), transmission electron microscope (TEM) and electron backscatter diffraction (EBSD) were used in this work.

2. Experimental study

The materials used in this investigation were 5 mm thick plates of AA2024-T351 and AA7075-T651 with a surface region of 300 mm × 40 mm. The chemical compositions of the two BMs are displayed in Table 1. The kinetics of contamination absorption and desorption were measured using a Sievert's type apparatus with calibrated volumes. The fillings were taken out manually from AA2024 BM and the NZ of the joint at atmospheric environment. A sample mass of approximately 50 mg and temperature of 623 K was employed in the measurements. A hydrogen pressure of 20 bar and 0.8 bar was used for absorption and desorption, respectively [31]. Compared to the hydrogen concentration of AA2024 BM (1.6 wt%), low hydrogen concentration about 0.9 wt% is found in the NZ. The gas contamination is associated with the formation of oxidation and intermetallics. Low gas contamination can reduce the formation of oxides and make microcracks less likely to occur during deformation, thus contributing to improve performance [32]. The FSW process was carried out using the FSW machine (FSW-LM-AM16-2D) with a butt welding configuration. AA2024 and AA7075 were placed on the AS and RS, respectively. The tool was rotated in the counterclockwise direction. The tool shoulder plunge depth was 0.03 mm, the rotational speed of 1495 rpm and welding speed of 187 mm/min were adopted to carry out this welding process, which is the previous optimal parameters [30]. The tool had a taper thread pin with 5 mm length accompanied by a shoulder of 15 mm diameter and the tilt angle was 2.5° during FSW.

Samples for the macro and microstructural investigation were cut from the transverse cross section of the dissimilar joint perpendicular to

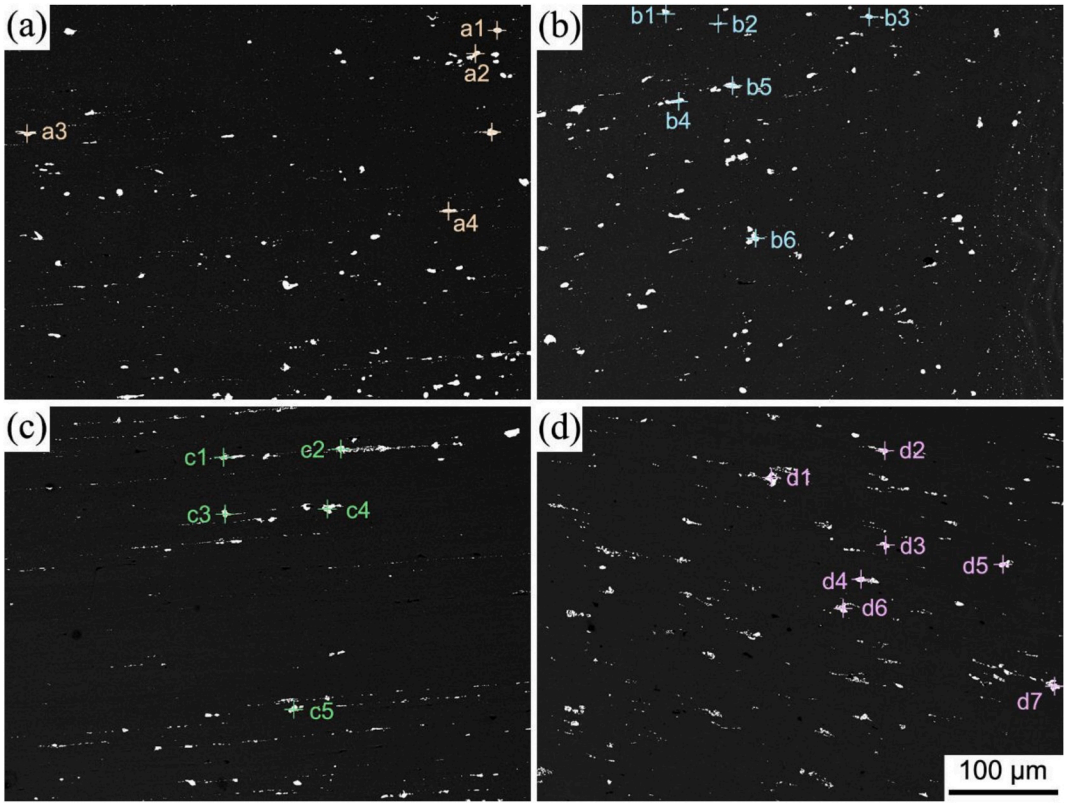

Fig. 3. BSE images (a) AA2024 BM, (b) AS-TMAZ, (c) AA7075 BM and (d) RS-TMAZ.

Table 2
Concentrations of elements acquired by EDS analysis (at%) of the two BMs and TMAZ (BSE images in Fig. 3).

Location	a	AA2024		b	AS-TMAZ		c	AA7075		d	RS-TMAZ		
	Al	Zn	Cu	Mg	Fe	Mn	Location	Al	Zn	Cu	Mg	Fe	Mn
a1	50.0	0.5	24.9	24.6	–	–	c2	75.7	1.6	4.1	0.6	18.0	–
a2	66.7	–	20.5	–	8.8	4.1	c3	64.8	0.7	20.4	0.3	13.8	–
a3	56.3	0.5	20.9	22.3	–	–	c4	65.9	0.9	19.6	0.4	13.2	–
a4	67.5	–	18.3	0.4	8.8	5.0	c5	75.8	1.7	4.1	0.3	18.2	–
b1	70.2	–	19.0	–	8.3	2.5	d1	75.6	1.8	4.1	0.4	18.2	–
b2	80.5	–	12.9	1.2	5.4	–	d2	69.4	1.3	17.3	0.9	11.1	–
b3	86.9	–	7.7	5.4	–	–	d3	75.8	1.6	4.1	0.3	18.3	–
b4	50.2	0.6	24.7	24.4	–	–	d4	75.7	1.6	4.2	0.3	18.2	–
b5	72.0	–	5.5	0.3	13.2	9.0	d5	87.6	2.4	4.4	2.6	3.0	–
b6	95.4	–	2.8	1.8	–	–	d6	65.3	0.7	20.3	–	13.7	–
c1	66.8	0.8	17.8	–	14.5	–	d7	69.4	1.2	17.3	0.9	11.2	–

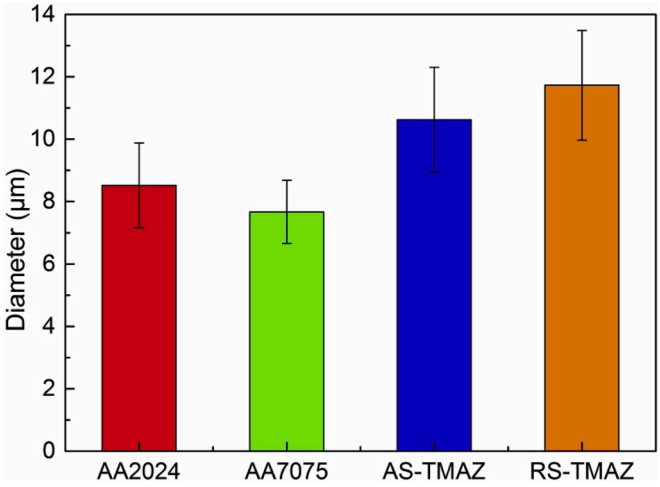

Fig. 4. Quantitative data on the average diameter of second number particles in the BMs as well as TMAZ. The data presented were obtained from an approximate region of 1.5 × 5 mm^2.

the welding direction (WD). A mirror finish was acquired for microstructure analysis by conducting the standard polishing procedure. The polished samples were corroded with Keller's reagent (HF: HCl: HNO_3: deionized water = 2 mL: 3 mL: 5 mL: 190 mL) for 40 s. X-ray diffractometer (XRD, Rigaku D/max 2500 PC) was used to recognize the alloy phases by adopting monochromatic CuKα radiation (λ = 0.1542 nm) with a step size of 0.01° and a time step of 0.1 s. The field emission scanning electron microscopy (FESEM, JEOL JSM-7800F) equipped with an energy dispersive spectroscopy (EDS) was employed to analyze the chemical composition of the samples. Furthermore, image processing and analyses were executed using Image J and Image Pro-Plus software to calculate the size of second phase particles. The transmission electron microscope (TEM) samples of the TMAZ were selected along the WD and cut into small pieces with the thickness of 1.5 mm. Then they were ground to a thickness of 60 μm and rushed into 3 mm in diameter. Finally, they were electropolished in a 25% HNO_3 methanol solution at −30 °C using the twin-jet technique. The precipitates phases were observed by using TEM (FEI TECNAI G2 F20), operated at 200 kV. The electron backscatter diffraction (EBSD) mapping was performed on a TESCAN MIRA3 SEM equipped with a HKL-EBSD system using a step size of 2 μm to investigate the grain structure. The EBSD samples were electropolished in an electrolyte (10 vol% perchloric acid: 90 vol% ethanol) at 2–5 °C and 15 V for 100 s.

Vickers micro-hardness tests were conducted using Vickers hardness tester (MH-5L). The hardness profile for each specimen was performed along the cross section perpendicular to the WD using a load of 200 gf with a dwell time of 10 s. The distance between each indentation was set to 1 mm.

3. Results and discussion

3.1. The cross section microstructure of the joint

The metallographic images of the as-received BMs are illustrated in Fig. 1a and b. It can be observed that both of the two BMs consists of typically elongated grains and the grain width of AA2024 BM is higher than that of AA7075 BM along the normal direction (ND). Fig. 1c exhibits the typical macroscopic view of the cross-section in the dissimilar FSW joint and different zones appear after corrosion with Keller's reagent. The dark area and the light area correspond to AA2024 and AA7075, respectively. It can be observed that the NZ in the joint has a basin shape. Compared to the two BMs (Fig. 1a and b), the grain structure in the TMAZ (Fig. 1d–g) displays a bending characteristic, and the degree of grain curvature in the RS-TMAZ are more pronounced than that in the AS-TMAZ. As shown in Fig. 1d–g, the boundary in the RS-TMAZ is not as clear as that in the AS-TMAZ, and the width of the AS-TMAZ (Fig. 1d and f) is smaller than that of the RS-TMAZ (Fig. 1e and g). This is attributed to plastic deformation during FSW. A cavity can be generated when the FSW tool is plunged into the welded materials. Since the linear speed of the material on the RS is equal to the difference value between the rotational speed and the welding speed, the linear speed of the material on the RS is much lower than that on the AS. Thus, the boundary is unclear and wide on the RS.

3.2. Phase analysis

XRD analysis was employed to obtain the information about the phases in the BMs and the corresponding TMAZ. As shown in Fig. 2, XRD patterns show the sharp and strong peaks corresponding to Al matrix and several weaker peaks of other constituent particles. Evidently, Al_2Cu, Al_2CuMg, AlCuMg and Al_7Cu_2Fe constituent particles are detected in AA2024 BM, while $MgZn_2$ and Al_7Cu_2Fe constituent particles present in AA7075 BM. Besides, it should be noted that the peak intensity of the small angles in the AS-TMAZ and the intensity of $MgZn_2$ peaks in the RS-TMAZ are lower than that of the corresponding BMs, which indicates that these constituent particles are dissolved in the corresponding TMAZ. This is in accordance with the results of Navaser and Atapour [33].

It is worth noting that the phases less than 5 wt% can't be detected by XRD [34]. Thus, the EDS analysis was employed to further identify the precipitated particles. The BSE images of the BMs and the corresponding TMAZ are shown in Fig. 3 and the EDS analysis results are summarized in Table 2. For the two BMs (Fig. 3a and c), the precipitated particles are aligned with the rolling direction. AA2024 BM mainly contains Al_2CuMg and Al_7Cu_2Fe constituent particles, while Al–Cu–Fe and Al–Zn–Cu–Fe constituent particles are distributed in the AA7075 BM. Al–Cu–Fe particles are usually formed under the condition of appreciable levels of

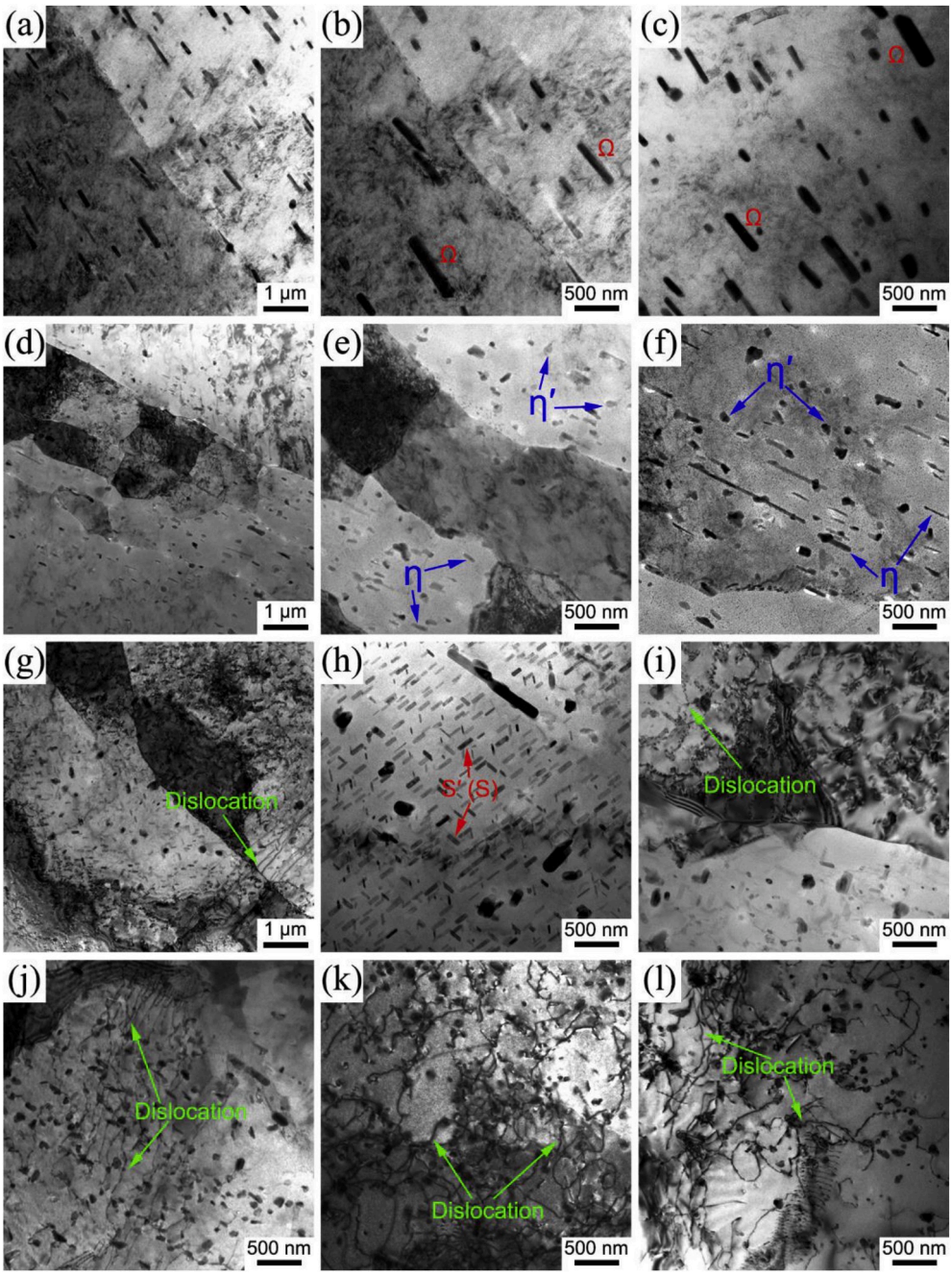

Fig. 5. TEM bright-field images of (a–c) AA2024 BM, (d–f) AA7075BM, (g–i) AS-TMAZ and (j–l) RS-TMAZ.

iron (viz. ~0.5 wt%) [35]. These constituent particles are not dissolved during the heat treatment and some coarse precipitates can be formed during solidification. Pitting and the development of initial corrosion damage are nominally associated with some fraction of the constituent particles in the high strength aluminum alloys [36,37]. The EDS analysis results on these particles in Table 2 indicate that Al–Cu–Fe, Al–Cu–Mg–Fe, Al–Cu–Mg and Al–Cu–Fe–Mn constituent particles present in the AS-TMAZ, and Al–Cu–Fe, Al–Zn–Cu–Fe and Al–Zn–Mg–Cu–Fe constituent particles are distributed in the RS-TMAZ. Apparently, many Cu-rich constituent particles are generated in the AS-TMAZ, while Zn-rich constituent particles are present in the RS-TMAZ. This can be attributed to the imposition of high temperature and small plastic deformation in the TMAZ during FSW.

Fig. 4 exhibits the quantitative data associated with the size and number density of second phase particles in the microstructure of two BMs and TMAZ. It should be pointed out that only particles larger than 2.37 (±0.45) μm were quantified by image processing. As demonstrated in Fig. 4, the average diameter of the particles in the TMAZ increases slightly as compared to those of the corresponding BMs, indicating that these precipitated particles in the AS-TMAZ and RS-TMAZ are coarsened in comparison with the corresponding BMs due to the thermal cycle produced by the friction between the FSW tool and the welded materials.

Both AA2024 and AA7075 BMs are precipitation-hardened aluminum alloys. A softened region around the weld is formed during FSW. The observations of typical precipitate distributions for the BMs and the corresponding TMAZ, as identified by TEM bright-field images, are shown in Fig. 5. It is well known that the sequence of the precipitate phases in the Al–Cu–Mg alloys is as follows [15]: supersaturated solid solution (SSS) → Guinier-Preston-Bagaryatsky (GPB) zone → θ″ → θ′ → θ

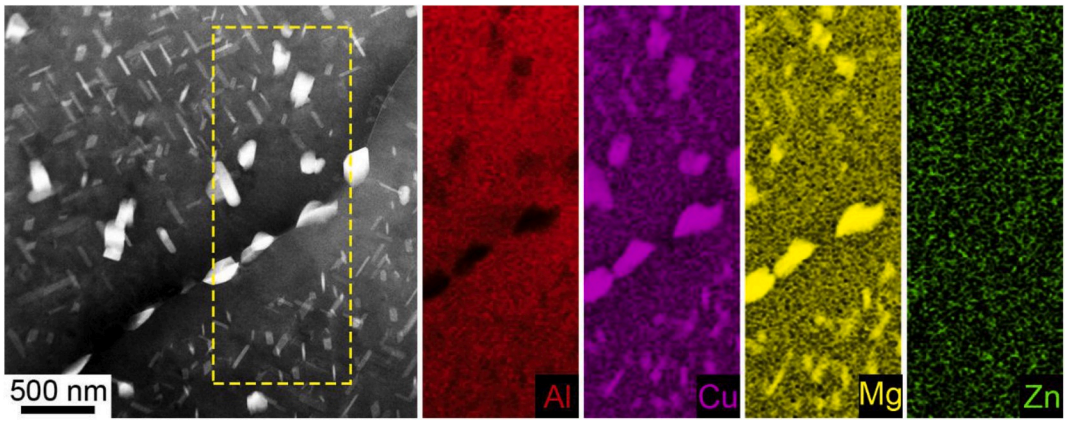

Fig. 6. TEM elemental mapping images of AS-TMAZ.

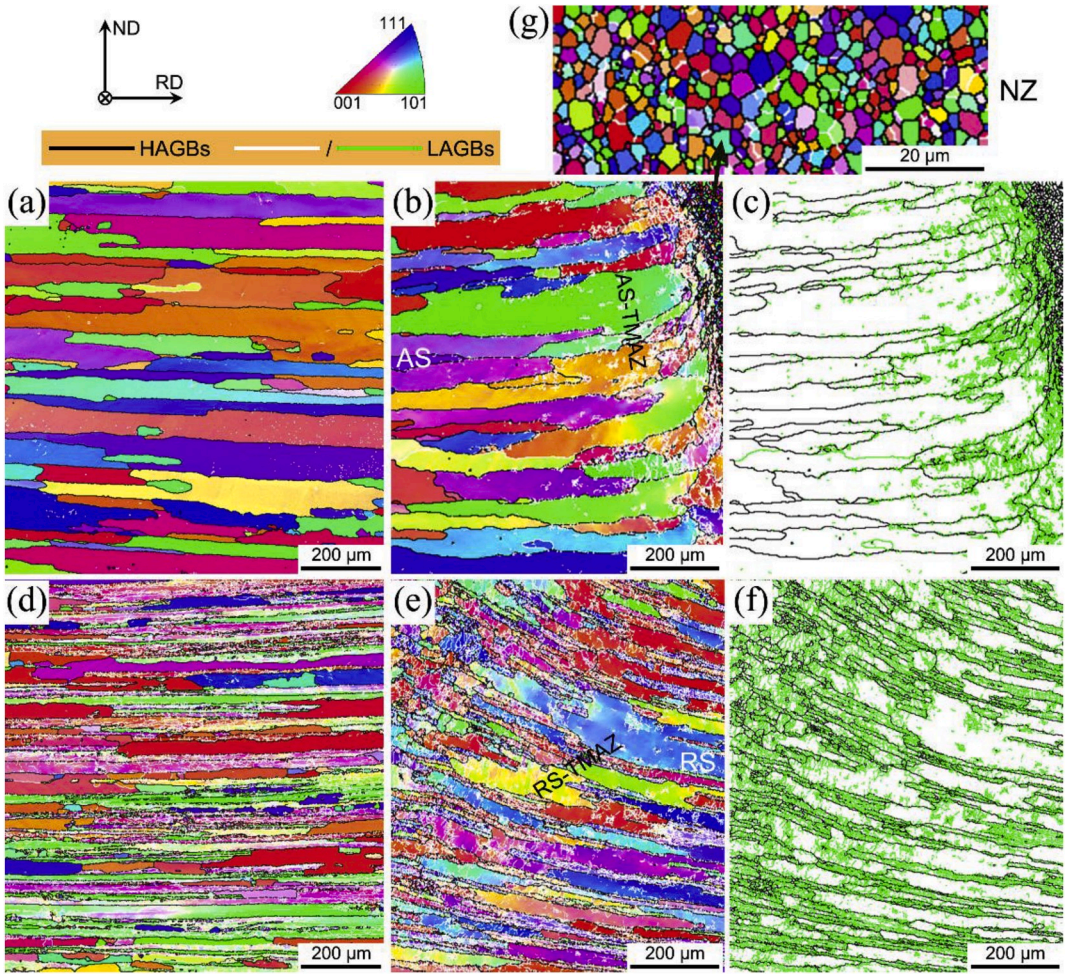

Fig. 7. Inverse pole figure (IPF) maps (a) AA2024 BM, (b) AA7075 BM, (c and d) AS-TMAZ, (e and f) RS-TMAZ and (g) NZ.

phase (Al_2Cu) and SSS → GPB zone → S′ → S phase (Al_2CuMg), where SSS represents the supersaturated solid solution. In the AA2024-T351 BM, GPB zones are the strengthening precipitates, which are hardly observed in traditional TEM images. However, they can be detected by diffuse streaks in the diffraction pattern [38], which also has been confirmed by Zhang et al. [39]. The microstructure of AA2024 BM (Fig. 5a–c) is characterized by a large number of rod-like phases. These phases are Ω ($Al_{20}Cu_2Mn_3$) phases with a typical size of 50–100 nm across and up to 500 nm in length [40]. Fig. 5h shows high fraction of S′ (S) phases with small size present in the AS-TMAZ, in agreement with the observation by Genevois et al. [38]. It can be clearly observed from the TEM elemental mapping images in Fig. 6 that coarsening precipitate phases are formed in the AS-TMAZ. Furthermore, we can also draw an obvious conclusion that these coarsening phases are mainly Cu–Mg--containing particles.

For the 7xxx series aluminum alloys Al–Zn–Mg-(Cu) alloys, the usual precipitation sequence can be summarized as [41]: SSS → GP zone → metastable η′ ($Mg(Zn,Al,Cu)_2$) → stable η ($MgZn_2$). It can be seen from

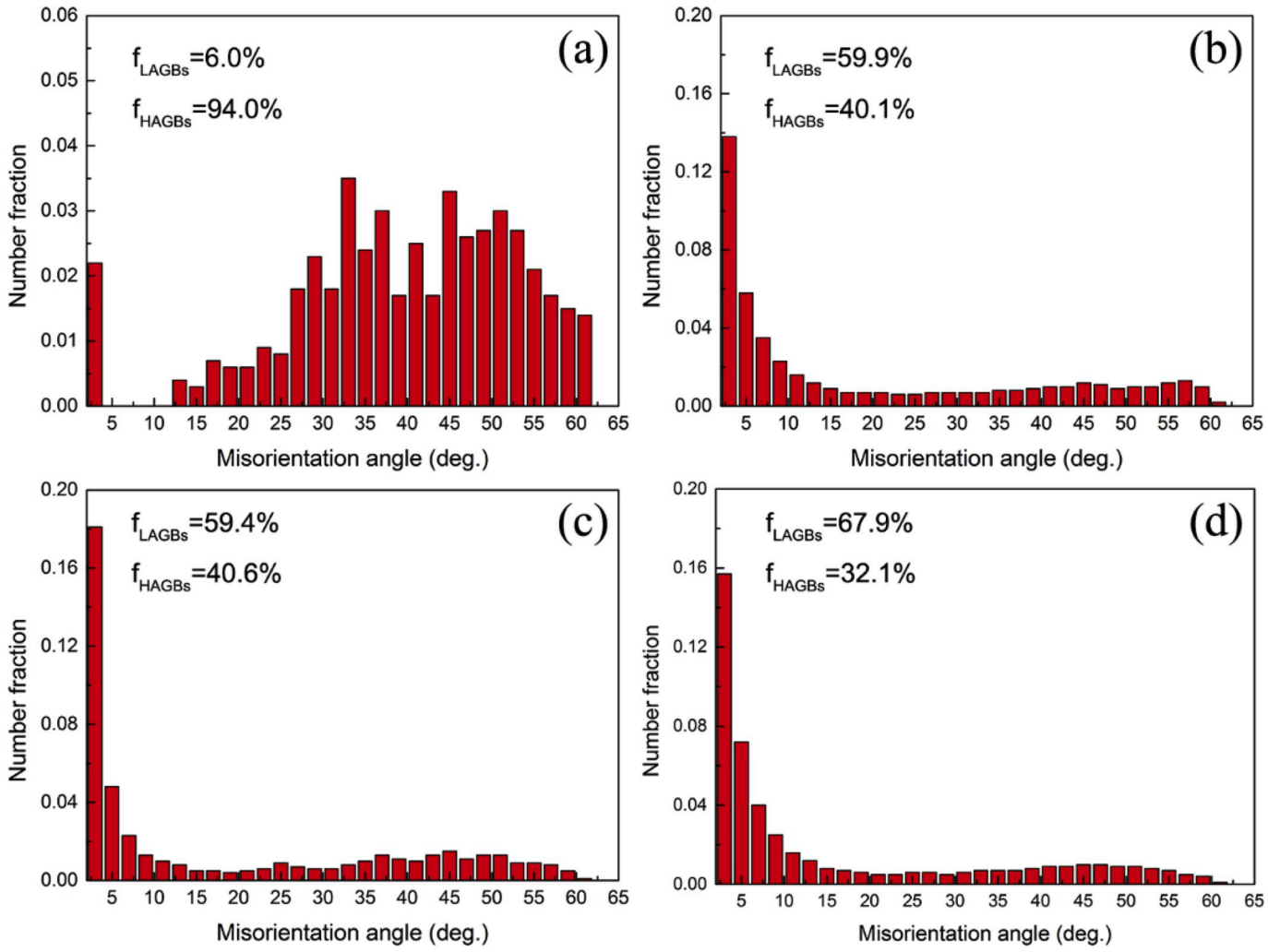

Fig. 8. Misorientation angle distributions (a) AA2024 BM, (b) AS-TMAZ, (c) AA7075 BM and (d) RS-TMAZ.

Fig. 5d–f that AA7075 BM mainly consists of η′ and η precipitates, which are uniformly distributed within the grains and at the grain boundaries. A number of small precipitation phases are distributed in the RS-TMAZ (Fig. 5j-l). The precipitate distribution in the AS-TMAZ (Fig. 5g–i, Fig. 6) and RS-TMAZ (Fig. 5j-l) is inhomogeneous, showing that the AS-TMAZ contains both coarse and fine precipitates while only small size of phases can be detected in the RS-TMAZ. The precipitates in the TMAZ experience severe coarsening and partial dissolution because of the high peak temperature caused by FSW, while the fine precipitates originate from the heterogeneous re-precipitation during cooling stage after welding. Besides, the TEM images in Fig. 5g-l demonstrate some highly dense dislocations and density gradient of dislocations in the AS-TMAZ and RS-TMAZ. The regions with higher density of dislocations, which are more thermodynamically unstable, are more sensitive to corrosion.

The TMAZ, characterized by a highly deformed structure, is generated located between the HAZ and the NZ. The elongated grains resulting from the BMs are preserved and the grains near the NZ are distorted through plastic deformation under the action of the tool. Therefore, a large number of dislocations are generated in the TMAZ, indicating that plastic deformation has been introduced. It is clearly observed that AS-TMAZ contains some sparse dislocations (Fig. 5g and i) and highly dense dislocations with some network structures can be found in the RS-TMAZ (Fig. 5j-l).

3.3. Grain structure

Fig. 7 illustrates the EBSD analysis results of the two BMs and the corresponding TMAZ, which clearly implies that the grain structures are significantly different between the BMs and the corresponding TMAZ. As shown in Fig. 7a and d, the two BMs consist of some typically rolling grain structures. During the FSW process, the microstructural evolution in the welded zone is very complicated, which is mainly concurrent with the heat input and plastic deformation. It has been reported that the decreasing sequence of peak temperature in the welded-affected zone is: NZ, TMAZ and HAZ [42]. Significant friction heat and violent plastic deformation could result in dynamic recrystallization in the NZ, producing conspicuously refined grains (Fig. 7g). Although recrystallization hardly occurs in the TMAZ, it still undergoes plastic deformation and thermal cycle to some extent, altering its initial microstructure. As displayed in Fig. 7b–c and 7e-f, many sub-grains associated with a large number of low angle grain boundaries (LAGBs, $2 < \theta < 15°$) can be observed in the AS-TMAZ and RS-TMAZ. According to the misorientation angle distribution data in Fig. 8, the LAGBs in both AS-TMAZ and RS-TMAZ are obviously increased due to the heterogeneous heat and deformation caused by the rotated tool.

3.4. Texture variation

Based on our previous researches, the dominating {001}100 Cube and slight {111}110 γ-fibre texture components can be found in the

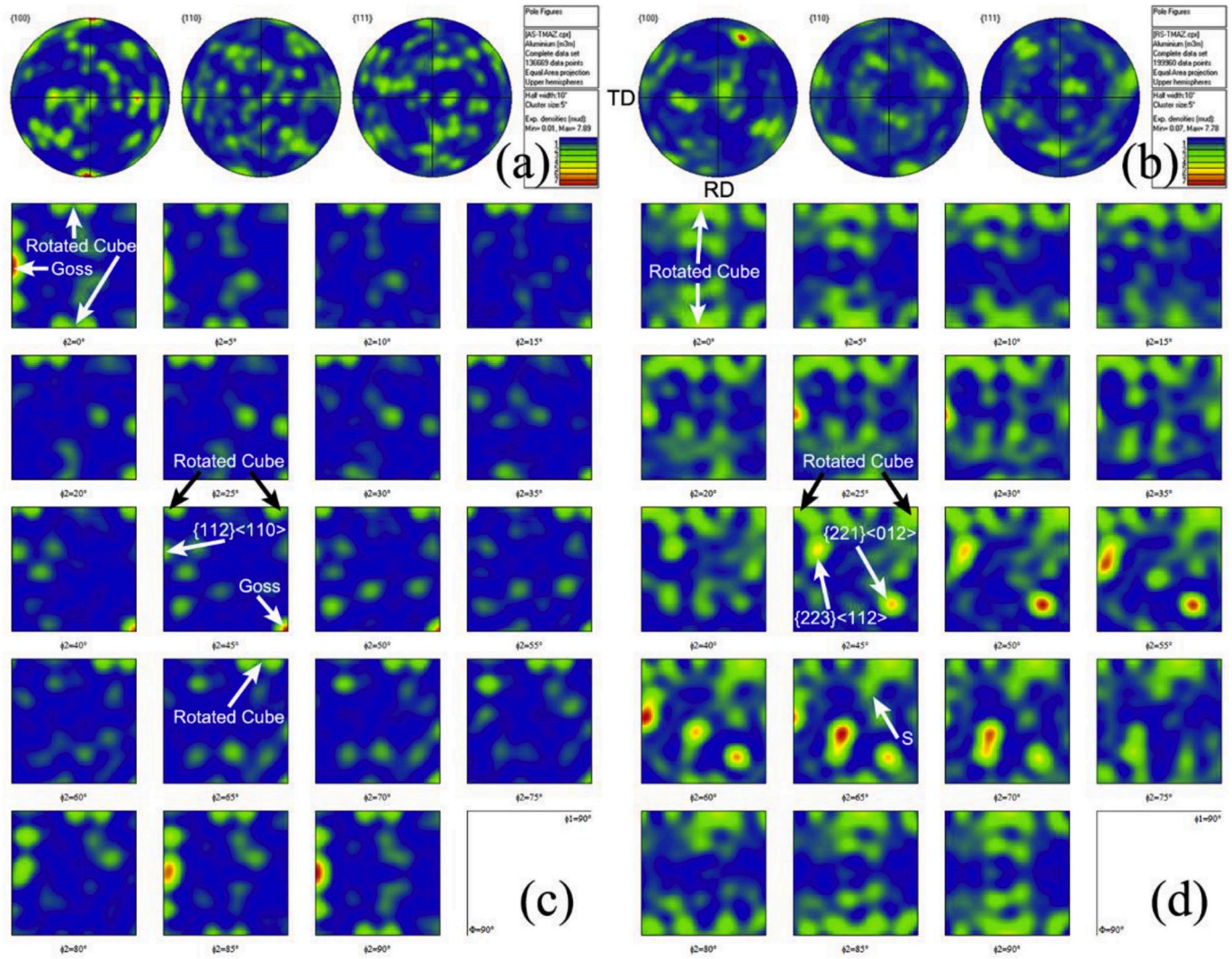

Fig. 9. {100}, {110} and {111} PFs and ODFs: (a) and (c) AS-TMAZ; (b) and (d) RS-TMAZ.

AA2024 BM, while {110}112 Brass, {123}634 S and slight {112}111 Cu texture components are presented in the AA7075 BM [7,43]. Fig. 9 exhibits the {100}, {110} and {111} pole figures (PFs) and orientation distribution functions (ODFs) of AS-TMAZ and RS-TMAZ. The PFs demonstrate that asymmetric crystallographic textures are distributed in the AS-TMAZ and RS-TMAZ, which is due to the fact that the heterogeneous plastic flow occurs during FSW. As shown in Fig. 9a and c, the AS-TMAZ can be characterized as the {001}110 Rotated Cube, {011} 100 Goss and slight {112}110 texture components. It can be clearly observed from Fig. 9b and c that the RS-TMAZ contains {001}110 Rotated Cube, {123}634 S, {223}112 and {221}012 texture components.

The above results demonstrate that the textures in the AS-TMAZ and RS-TMAZ are different as compared to the as-received BMs, suggesting that complicated plastic flow takes place during stirring and friction. In the AS-TMAZ, the entire texture strength is slightly higher that the AA2024 BM [7]. The original {001}100 Cube texture component rotate into the {001}110 Rotated Cube texture component by means of the activity of {111}110 slip system during FSW. The texture variation in the RS-TMAZ of the dissimilar joint is different from that in the AS-TMAZ. The overall texture strength is weaker than the corresponding AA7075 BM [7]. The initial {110}112 Brass texture is disappeared, while new texture components including {001}110 Rotated Cube, {223}112 and {221}012 are formed. It is worth noting that the {221}012 is generated, which is an uncommon shear component, resulting from that the shear strain is produced in the RS-TMAZ during FSW [2]. This orientation is close to the conventional shear components such as {111}112 and {111}110, which is in accordance with the literature [2,44–46].

3.5. Microhardness

Microhardness tests were performed across the cross-section of the dissimilar FSW joint perpendicular to the WD. The distance of hardness indentations of 1 mm was set on the center line of the thickness of the joint. As shown in Fig. 10a, a profile of typical W shape is observed, which usually presents in case of FSW joint of the heat treatable aluminum alloys. However, the hardness profile is asymmetric due to the different BMs. It is observed from Fig. 10a–b and 10e-f that the hardness value of AA2024 and AA7075 is 160.4 ± 2.7 and 179.4 ± 2.62 HV, respectively. Due to the narrow zone and the heterogeneous microstructure in the TMAZ, the hardness test was carried out in the local area of the TMAZ with a distance of 50 μm. It is concluded from Fig. 10c–d and 10e-f that the hardness value of AS-TMAZ and RS-TMAZ is lower than that of the corresponding BMs. The hardness profile depends mainly upon the precipitate distribution and only slightly on the grain and dislocation structures [38]. During FSW, the TMAZ near the NZ experiences high thermal cycle and severe plastic deformation, and then the precipitate phases coarsen or dissolution (Fig. 5g-l), which

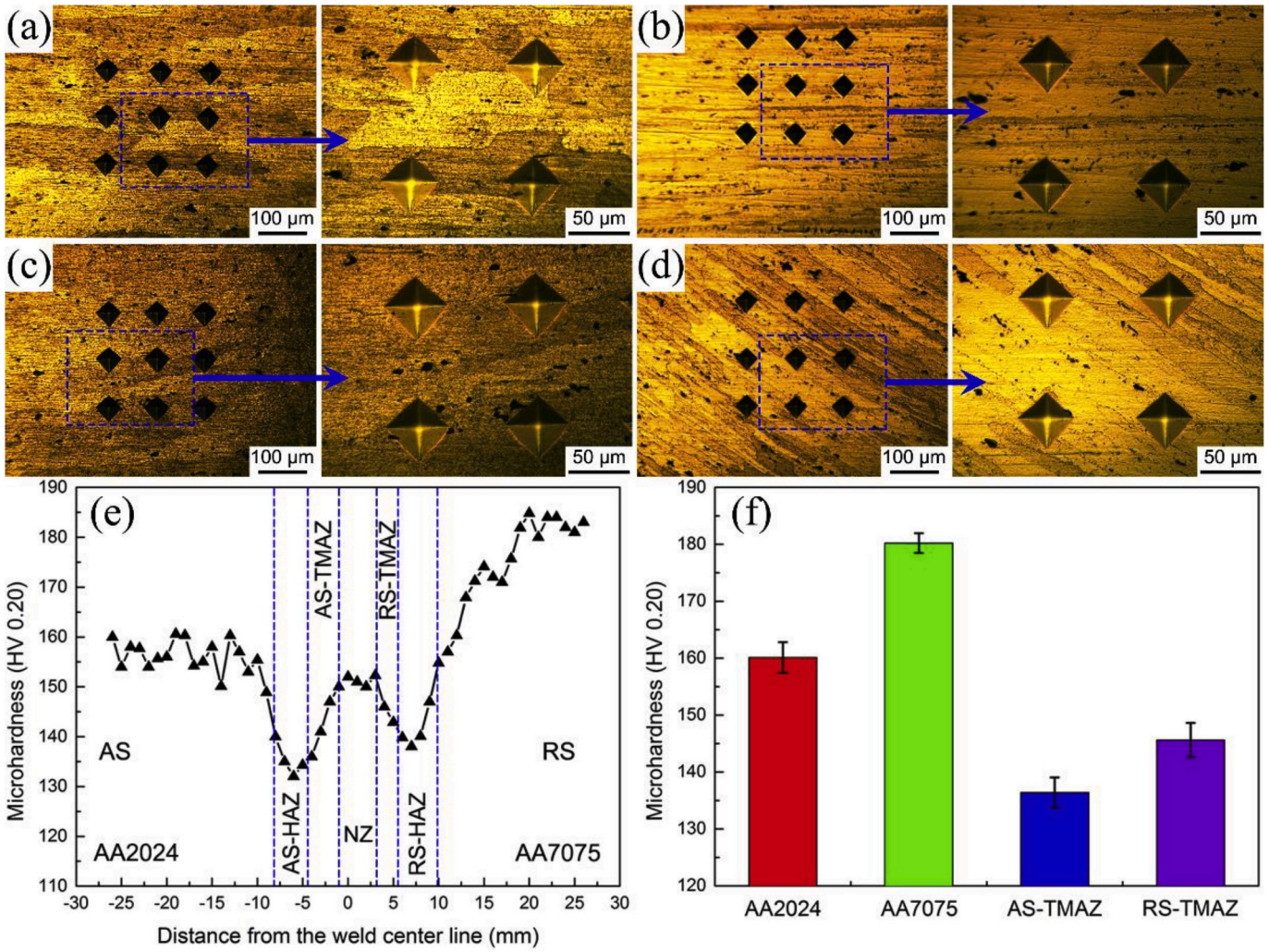

Fig. 10. OM micro-graphs with hardness indentation (a) AA2024 BM, (b) AA7075 BM, (c) AS-TMAZ, (d) RS-TMAZ, (e) hardness profile of the dissimilar joint and (f) statistical results of hardness value of the two BMs and the corresponding TMAZ.

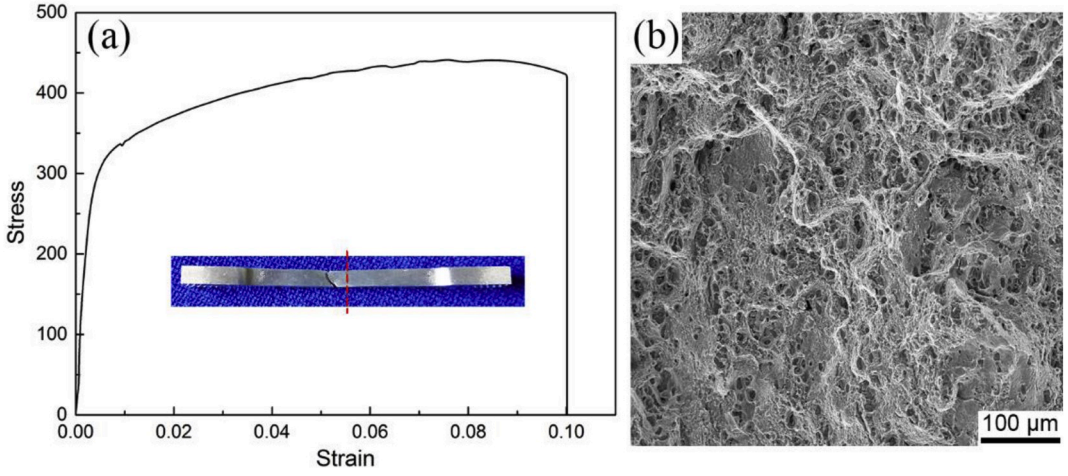

Fig. 11. Tensile results: (a) tensile curves and fracture location of the joint and (b) fracture morphology.

reduces the strengthening effect of the second phases at this region. Finally, resulting in the softening in the TMAZ.

The tensile test results and fracture features of the joint are shown in Fig. 11a and b. It can be concluded from Fig. 11a that the yield strength, ultimate tensile strength and elongation of the joint are 301 MPa, 441 MPa and 10%, respectively. Compared to our precious work [7], higher mechanical properties are obtained. We find that the joint is fractured close to the TMAZ (Fig. 11b), which is located in the minimum hardness

region of the joint (Fig. 10e). This can be attributed to the coarsening and partial dissolution of the precipitated phases occurring in the TMAZ (Figss. 4–6), which results from the plastic deformation and thermal cycle during FSW. The fracture morphology of the joint is shown in Fig. 11b, we can observe that the fracture surface of the joint is characterized by a large number of dimples and partially smooth surfaces (cleavage surfaces), indicating a mixed fracture mode of ductile-brittle.

In the present study, XRD, SEM/EDS, TEM and EBSD techniques were utilized to evaluate the microstructure and texture evolution within the TMAZ. These microstructural factors, such as precipitate phase particles [47] and grain structure [48] can affect the corrosion behavior. Thus, the corrosion behavior of the TMAZ in the dissimilar FSW AA2024/7075 joints can be studied in the future work.

4. Conclusions

In this investigation, the microstructure evolution of the TMAZ in dissimilar friction stir welding AA2024/7075 joints was thoroughly investigated. The main conclusions can be drawn as follows:

1) Al_2Cu, Al_2CuMg, AlCuMg and Al_7Cu_2Fe constituent particles are detected in AA2024 BM, while $MgZn_2$ and Al_7Cu_2Fe constituent particles present in AA7075 BM.
2) Many Cu-rich constituent particles are generated in the AS-TMAZ, while Zn-rich constituent particles are presented in the RS-TMAZ, which is mainly determined by the corresponding BMs at the AS and RS.
3) Grain bending occurs in the TMAZ, and the degree of grain curvature in the RS-TMAZ are more pronounced than that in the AS-TMAZ. Many dislocations and sub-grains associated with a large number of LAGBs can be found in the AS-TMAZ and RS-TMAZ.
4) The entire texture intensity is increased in the AS-TMAZ but is decreased in the RS-TMAZ as compared to the corresponding BMs. The original texture components are changed and some new shear components can be produced as a result of the severe shear deformation during FSW.
5) The hardness value of the AS-TMAZ and RS-TMAZ is lower than that of the corresponding BMs. The fracture location of the joint is in the minimum hardness region due to the precipitated particles coarsening, which results from the thermal cycle produced by the friction and stirring of the FSW tool.
6) The TMAZ is an unsubstantial location in the dissimilar FSW AA2024/7075 joints due to the low hardness resulting from the coarsened phase particles.
7) The microstructure such as precipitated phase particles and texture components of the TMAZ in the FSW joints mainly depend on the type and initial status of the BMs.

Declaration of competing interest

We declare that we do not have any commercial or associative interest that represents a conflict of interest in connection with the work submitted.

Acknowledgements

The “National Natural Science Foundation of China” (No. 51421001) and “Fundamental Research Funds for the Central Universities” (No. 2018CDJDCL0019 and No. 2020CDJQY-A003) are greatly acknowledged for financial support. We also greatly acknowledge the Electron Microscopy Center of Chongqing University for providing SEM and TEM test channel.

References

[1] H.J. Aval, Microstructure and residual stress distributions in friction stir welding of dissimilar aluminium alloys, Mater. Des. 87 (2015) 405–413.
[2] M.M. Moradi, H.J. Aval, R. Jamaati, S. Amirkhanlou, S. Ji, Microstructure and texture evolution of friction stir welded dissimilar aluminum alloys: AA2024 and AA6061, J. Manuf. Process. 32 (2018) 1–10.
[3] G. Çam, G. İpekoğlu, Recent developments in joining of aluminum alloys, Int. J. Adv. Manuf. Technol. 91 (2017) 1851–1866.
[4] T. Dursun, C. Soutis, Recent developments in advanced aircraft aluminium alloys, Mater. Des. 56 (2014) 862–871.
[5] R.S. Mishra, Z. Ma, Friction stir welding and processing, Math. Sci. Eng. R 50 (2005) 1–78.
[6] R. Nandan, T. DebRoy, H. Bhadeshia, Recent advances in friction-stir welding–process, weldment structure and properties, Prog. Mater. Sci. 53 (2008) 980–1023.
[7] C. Zhang, G. Huang, Y. Cao, Y. Zhu, Q. Liu, On the microstructure and mechanical properties of similar and dissimilar AA7075 and AA2024 friction stir welding joints: effect of rotational speed, J. Manuf. Process. 37 (2019) 470–487.
[8] M. Mohammadi-pour, A. Khodabandeh, S. Mohammadi-pour, M. Paidar, Microstructure and mechanical properties of joints welded by friction-stir welding in aluminum alloy 7075-T6 plates for aerospace application, Rare Met. (2016) 1–9.
[9] J.L. Meseguer-Valdenebro, E.J. Martinez-Conesa, J. Serna, A. Portoles, Influence of the welding parameters on the heat affected zone for aluminium welding, Therm. Sci. 20 (2016) 643–653.
[10] E. Siewert, G. Wilhelm, M. Häßler, J. Schein, T. Hanson, M. Schnick, et al., Visualization of gas flows in welding arcs by the Schlieren measuring technique, Weld. J. 93 (2014) 1S–5S.
[11] C. Selcuk, Joining Processes for Powder Metallurgy Parts, Advances in Powder Metallurgy: Elsevier, 2013, pp. 380–398.
[12] P. Liu, S. Sun, S. Xu, Y. Li, G. Ren, Microstructure and properties in the weld surface of friction stir welded 7050-T7451 aluminium alloys by laser shock peening, Vacuum 152 (2018) 25–29.
[13] C. Liu, B. Zhang, Z. Ma, G. Teng, L. Wei, W. Zhou, et al., Effects of pre-aging and minor Sc addition on the microstructure and mechanical properties of friction stir processed 7055 Al alloy, Vacuum 149 (2018) 106–113.
[14] C. Zhang, L. Cui, D. Wang, Y. Liu, C. Liu, H. Li, The heterogeneous microstructure of heat affect zone and its effect on creep resistance for friction stir joints on 9Cr–1.5 W heat resistant steel, Scripta Mater. 158 (2019) 6–10.
[15] Z. Ma, A. Feng, D. Chen, J. Shen, Recent advances in friction stir welding/processing of aluminum alloys: microstructural evolution and mechanical properties, Crit. Rev. Solid State 43 (2018) 269–333.
[16] H. Zhang, Y. Lu, Y. Huang, A. Feng, Z. Qin, X. Lu, Joining of Zr51Ti5Ni10Cu25Al9 BMG to aluminum alloy by friction stir welding, Vacuum 120 (2015) 47–49.
[17] A. Heidarzadeh, R.V. Barenji, V. Khalili, G. Güleryüz, Optimizing the friction stir welding of the α/β brass plates to obtain the highest strength and elongation, Vacuum 159 (2019) 152–160.
[18] F. Zarghani, S. Mousavizade, H. Ezatpour, G. Ebrahimi, High mechanical performance of similar Al joints produced by a novel spot friction welding technique, Vacuum 147 (2018) 172–186.
[19] V. Magalhães, C. Leitão, D. Rodrigues, Friction stir welding industrialisation and research status, Sci. Technol. Weld. Join. 23 (2018) 400–409.
[20] C. Zhang, G. Huang, Y. Cao, Y. Zhu, W. Li, X. Wang, et al., Microstructure and mechanical properties of dissimilar friction stir welded AA2024-7075 joints: influence of joining material direction, Mater. Sci. Eng., A (2019), 138368.
[21] Z. Chenghang, H. Guangjie, C. Yu, L. Wei, L. Qing, EBSD analysis of nugget zone in dissimilar friction stir welded AA2024-AA7075 joint along weld thickness, Rare Met. Mater. Eng. 48 (2019) 3161–3166.
[22] J. Kang, J. Li, Z. Feng, G. Zou, G. Wang, A. Wu, Investigation on mechanical and stress corrosion cracking properties of weakness zone in friction stir welded 2219-T8 Al alloy, Acta Metall. Sin. 52 (2016) 60–70.
[23] S. Chen, X. Li, X. Jiang, T. Yuan, Y. Hu, The effect of microstructure on the mechanical properties of friction stir welded 5A06 Al Alloy, Mater. Sci. Eng., A 735 (2018) 382–393.
[24] R. Bertrand, H. Robe, D. Texier, Y. Zedan, E. Feulvarch, P. Bocher, Analysis of AA2XXX/AA7XXX friction stir welds, J. Mater. Process. Technol. 271 (2019) 312–324.
[25] M. Mahoney, C. Rhodes, J. Flintoff, W. Bingel, R. Spurling, Properties of friction-stir-welded 7075 T651 aluminum, Metall. Mater. Trans. A 29 (1998) 1955–1964.
[26] F. Liu, Z. Ma, Influence of tool dimension and welding parameters on microstructure and mechanical properties of friction-stir-welded 6061-T651 aluminum alloy, Metall. Mater. Trans. A 39 (2008) 2378–2388.
[27] C. Rhodes, M. Mahoney, W. Bingel, R. Spurling, C. Bampton, Effects of friction stir welding on microstructure of 7075 aluminum, Scripta Mater. 36 (1997) 69–75.
[28] F. Liu, L. Fu, H. Chen, Microstructure evolution and fracture behaviour of friction stir welded 6061-T6 thin plate joints under high rotational speed, Sci. Technol. Weld. Join. 23 (2018) 333–343.
[29] S. Chen, X. Jiang, Texture evolution and deformation mechanism in friction stir welding of 2219Al, Mater. Sci. Eng., A 612 (2014) 267–277.
[30] C. Zhang, G. Huang, Y. Cao, X. Wu, X. Huang, Q. Liu, Optimization of tensile and corrosion properties of dissimilar friction stir welded AA2024-7075 joints, J. Mater. Eng. Perform. 28 (2019) 183–199.
[31] R. Checchetto, G. Trettel, A. Miotello, Sievert-type apparatus for the study of hydrogen storage in solids, Meas. Sci. Technol. 15 (2004) 127–130.

[32] E. Silva, D. Leiva, H. Pinto, R. Floriano, A. Neves, W. Botta, Effects of friction stir processing on hydrogen storage of ZK60 alloy, Int. J. Hydrogen Energy 43 (2018) 11085–11091.
[33] M. Navaser, M. Atapour, Effect of friction stir processing on pitting corrosion and intergranular attack of 7075 aluminum alloy, J. Mater. Sci. Technol. 33 (2017) 155–165.
[34] H. Sarlak, M. Atapour, M. Esmailzadeh, Corrosion behavior of friction stir welded lean duplex stainless steel, Mater. Des. 66 (2015) 209–216.
[35] N. Birbilis, M. Cavanaugh, R. Buchheit, Electrochemical behavior and localized corrosion associated with Al7Cu2Fe particles in aluminum alloy 7075-T651, Corrosion Sci. 48 (2006) 4202–4215.
[36] Z. Szklarska-Smialowska, Pitting corrosion of aluminum, Corrosion Sci. 41 (1999) 1743–1767.
[37] T. Hu, H. Shi, D. Hou, T. Wei, S. Fan, F. Liu, et al., A localized approach to study corrosion inhibition of intermetallic phases of AA 2024-T3 by cerium malate, Appl. Surf. Sci. 467 (2019) 1011–1032.
[38] C. Genevois, A. Deschamps, A. Denquin, B. Doisneau-Cottignies, Quantitative investigation of precipitation and mechanical behaviour for AA2024 friction stir welds, Acta Mater. 53 (2005) 2447–2458.
[39] Z. Zhang, B. Xiao, Z. Ma, Hardness recovery mechanism in the heat-affected zone during long-term natural aging and its influence on the mechanical properties and fracture behavior of friction stir welded 2024Al–T351 joints, Acta Mater. 73 (2014) 227–239.
[40] S. Cheng, Y. Zhao, Y. Zhu, E. Ma, Optimizing the strength and ductility of fine structured 2024 Al alloy by nano-precipitation, Acta Mater. 55 (2007) 5822–5832.
[41] A. Ghosh, M. Ghosh, G. Shankar, On the role of precipitates in controlling microstructure and mechanical properties of Ag and Sn added 7075 alloys during artificial ageing, Mater. Sci. Eng., A 738 (2018) 399–411.
[42] M. Imam, Y. Sun, H. Fujii, M. Ninshu, S. Tsutsumi, S. Ahmed, et al., Deformation characteristics and microstructural evolution in friction stir welding of thick 5083 aluminum alloy, Int. J. Adv. Manuf. Technol. 99 (2018) 663–681.
[43] C. Zhang, Y. Cao, G. Huang, Q. Zeng, Y. Zhu, X. Huang, et al., Influence of tool rotational speed on local microstructure, mechanical and corrosion behavior of dissimilar AA2024/7075 joints fabricated by friction stir welding, J. Manuf. Process. 49 (2020) 214–226.
[44] X. Xu, Y. Lu, F. Zheng, B. Chen, Microstructural investigation of friction-stir-welded 7005 aluminum alloy, J. Mater. Eng. Perform. 24 (2015) 4297–4306.
[45] B. Wang, B.-b. Lei, J.-x. Zhu, Q. Feng, L. Wang, D. Wu, EBSD study on microstructure and texture of friction stir welded AA5052-O and AA6061-T6 dissimilar joint, Mater. Des. 87 (2015) 593–599.
[46] M. Imam, V. Racherla, K. Biswas, H. Fujii, V. Chintapenta, Y. Sun, et al., Microstructure-property relation and evolution in friction stir welding of naturally aged 6063 aluminium alloy, Int. J. Adv. Manuf. Technol. 91 (2017) 1753–1769.
[47] M.F. Naeini, M.H. Shariat, M. Eizadjou, On the chloride-induced pitting of ultra fine grains 5052 aluminum alloy produced by accumulative roll bonding process, J. Alloys Compd. 509 (2011) 4696–4700.
[48] X. Zhang, X. Zhou, T. Hashimoto, J. Lindsay, O. Ciuca, C. Luo, et al., The influence of grain structure on the corrosion behaviour of 2A97-T3 Al-Cu-Li alloy, Corrosion Sci. 116 (2017) 14–21.